Influence of electrode fabrication process on nanocrystalline tin oxide electrochemical behaviour for high voltage SnO2/LNMO full cell Li-ion battery

Influence of electrode fabrication process on nanocrystalline tin oxide electrochemical behaviour for high voltage SnO_2/LNMO full cell Li-ion battery.

Daniele Versaci[1*], Georgia Kastrinaki[2], George Ganas[2], Dimitrios Zarvalis[2], George Karagiannakis[2], Julia Amici[1], Carlotta Francia[1], Silvia Bodoardo[1]

[1] *Politecnico di Torino, Department of Applied Science and Technology, Electrochemistry Group, Corso Duca degli Abruzzi, 24, 10129 Turin, Italia.*

[2] *Chemical Process and Energy Resources Institute, Center for Research and Technology Hellas, 57001, Thessaloniki, Greece*

*Corresponding authors:

Daniele Versaci, Tel.: +39 011 090 4789; E-mail address: daniele.versaci@polito.it;

KEYWORDS: SnO_2 nanoparticles, sol-gel synthesis, anodes, LNMO, Full cell, Li-ion battery

ABSTRACT

Tin oxide is one of the most promising anode materials to replace graphite in the next generation lithium-ion batteries thanks to its high theoretical specific capacity, low cost and large availability. Unfortunately, its large-scale application is still limited, due to marked capacity loss and poor cyclability. Recent findings demonstrated improved reversibility of the electrochemical reactions through the optimization of SnO_2 particles size. In this frame, the sol-gel method has proved to be one of the most interesting synthesis processes to obtain mono and polycrystalline SnO_2 particles, which guarantee higher reversibility of the conversion reaction. In this work, SnO_2 nanoparticles was

synthesized by sol-gel method, with an average size of 5 - 50 nm, depending on the post calcination temperature. Subsequently, the optimization of the electrode composition in terms of mass loading and binder allowed to achieve a specific capacity of 350 mAh g^{-1}, with a coulombic efficiency of 99.9 % after 100 cycles at high current rate of 0.75 A g^{-1}. Finally, the optimized and pre-lithiated SnO_2 anode was coupled with the high voltage $LiNi_{0.5}Mn_{1.5}O_4$ (LNMO) cathode in full-cell configuration, and the contribution of the voltage window and formation step to the final cell capacity was studied to determine the optimum conditions at which high cycling stability can be obtained.

1. Introduction

Nowadays, it is generally accepted that Li-ion battery technology can play a crucial role in the energy transition, facilitating decarbonization of the transportation sector and providing a pivotal contribution in the energy storage from intermittent solar and wind sources [1].

At the same time, for all these applications a battery system able to guarantee fast and safe charge is fundamental and strategic for the mass adoption and diffusion of these technologies [2][3][4].

However, it is generally accepted that the lithium-ion intercalation in graphite-based electrodes is one of the bottlenecks for the fast charging, limiting the performance of the battery and strongly affecting the safety of the system [5][6]. In addition, graphite has a theoretical specific capacity of 372 mAh g^{-1}, which cannot meet the future generations battery requirements [7][8].

In the last decades, different materials have been studied as alternative anodes for Li-ion battery such as alloys, conversion materials and metal oxides. However, many of these materials show some issues and drawbacks, such as poor cyclability, reduced operational potential, poor electronic conductivity, or high production cost, which have inevitably limited their diffusion and commercialization [8][9].

More recently, the use of hybrid materials such as silicon and graphite blends are among the most attractive options to increase energy density and achieve the targets set for next generation batteries. Electrodes with a variable percentage of silicon and graphite have been developed and are currently used in commercial lithium-ion batteries with the aim of increasing the specific capacity of the system [10][11]. However, the percentage of silicon is still low compared to that of graphite, and the limits associated with fast charging are not addressed yet. Furthermore, silicon is within the materials that are recognized as critical in the "Report on critical raw materials" by EU in 2020 [12]. For these reasons, there is a clear need to study and develop alternative anodic materials able to guarantee higher energy densities and good rate capabilities while being widely available.

In this frame tin dioxide (SnO_2) is one of the most valued materials for Li-ion battery (LIBs) anodes and has gained particular interest due to its low cost, high availability and above all, excellent electrochemical properties. It is indeed characterized by a high theoretical specific capacity (for alloying/de-alloying reaction ~782 mAh g^{-1} and for alloying/de-alloying and conversion reactions, ~1494 mAh g^{-1}) as well as an average charge and discharge potential of 0.5 V and 0.3 V vs. Li^+/Li [13][14][15]. Unfortunately, the widespread use of SnO_2 as anode has been strongly limited by its intrinsic low electronic conductivity, by the limited reversibility of the conversion reaction and the marked volume expansion during the alloying reaction. These drawbacks have been

partially overcome through material engineering, such as miniaturization of the particles and creation of hybrid materials, in which a carbonaceous material or carbon-based matrix limits the volumetric expansion and, at the same time, guarantees good electronic conductivity [16][17][18]. Therefore, many different nanostructured SnO_2 and composites have been reported in literature, such as SnO_2 and Sn/SnO_2 hybrids [19] with hollow structures, able to provide extra void space alleviating the stresses of Li de-/intercalation processes [20], thin carbon layer applied to the exterior surface of SnO_2 hollow spheres [21] as well as well-designed surface engineering of porous carbon coatings on $CNT@SnO_2$ composites that increased the Li ion diffusion through an open tunnel-like architecture [22]. The embedding of either Sn [23] or SnO_2 nanoparticles into porous carbon or carbon nano/micro spheres provided materials with high surface area allowing more surface lithium storage sites [24], while the fabrication of SnO_2 quantum dots on N-doped carbons significantly decreased the diffusion distance for ion/electrons improving the rate capability of the cell [25].

More recent researches intensively explored the complex reaction mechanism of Li storage in SnO_2 by in situ/in operando techniques in both liquid [26] and solid electrolytes [27] and validated that SnO_2 conversion/alloying reaction is a five step mechanism involving several different phases such as SnO_x, Li_8SnO_6, Li_2SnO_3, Li_xSn, Sn and Li_2O, depending on the lithiation potential. At the same time, it has been observed that the irreversible capacity during the first cycles and the poor cycling stability are ascribable to the aggregation of Sn particles into inactive clusters during charge/discharge processes. Such Sn coarsening-induced volume shrinkage is one of the main reasons for capacity fading thus, the repeated formation of very small Sn particles starting from nanosized and robust SnO_2 is still the most feasible way to obtain high capacity and stable cycling performances [28].

As a consequence, the SnO_2 anode performance in LiBs are strictly related to the variety of morphologies in which the material can be prepared, *i.e.* 1D [29], 2D [30], 3D [31], along with its particle size [32] and their distribution in confining matrices that limit their coalescence and improve their conductivity [33]. Unfortunately, such matrices usually lead to increase the content of the inert mass, which lowers the volumetric and gravimetric energy density of the final battery. It is almost certain that the breakthrough for SnO_2 as anode will require the design of nanocomposite electrode [34] materials, but currently most of the production processes appear complicated for scale-up.

Taking into account all these considerations, SnO_2 nanoparticles have been prepared by cost-effective and highly scalable sol-gel approach, followed by calcination at different temperatures. Sol-gel method has been chosen for its ability to provide fine dispersion of tin precursors limiting coarsening of nanoparticles [35], and resulting in narrow dispersion of SnO_2 NPs with an average size between 5-10 nm, (which can increase to 20 nm by post treatment). Besides, nanosizing of SnO_2 particles allows to maintain a high fraction of Sn/Li_2O interfaces, which strongly improves the reversible dis-/charge reactions [36].

Then, through the chemical-physical and morphological study of the particles obtained by sol-gel approach, the optimal post-treatment process has been identified in order to obtain finely dispersed SnO_2 nanoparticles with high surface area.

In a second step, the material with the best morphological properties has been studied from an electrochemical point of view as suitable anode material for LIBs. Particular attention is given to the engineering of the electrode by studying different slurry compositions, different mass loading and different binder/solvent couples. In fact, the impressive electrochemical performances of highly nanostructured SnO_2 electrodes are

often achieved at very low mass loadings (*i.e* 1.0 mg cm^{-2} or less), where the mass of the inert components (current collectors and separators) highly exceeds the one of the active material [37][38][39][40].

Finally, the electrochemical performances of the optimized SnO_2 electrode have been evaluated in a full cell configuration, coupling the tin oxide-based anode with a cobalt-free $LiNi_{0.5}Mn_{1.5}O_4$ (LNMO) cathode. LNMO is chosen because it is considered a good candidate for the next generation cobalt-free positive AMs, but its commercial application is still hindered by some drawbacks such as the dissolution of transition metals (*i.e.* Mn) and the electrolyte decomposition occurring at high operating potential [41], in particular if coupled with the graphite anode.

Hence the evaluation of the electrochemical performance of SnO_2 in a full cell configuration with high voltage cathode materials, is promising but has not fully been characterized yet.

2 Material and methods

2.1 Preparation of SnO_2 through sol-gel synthesis

SnO_2 nanoparticles were synthesized by a sol-gel method. Typically, 9 gr of $SnCl_4 \cdot 2H_2O$ (Sigma-Aldrich) were dissolved in 100 ml deionized water under stirring, NH_4OH (25%) was added up to pH 8 dropwise. The resulting solution was stirred for 2 hours and left in a closed flask for 24 hours before calcination. The calcination temperatures were 400, 700, 900 and 1000 °C for 2 hours (samples respectively named SnO_2-400, SnO_2-700, SnO_2-900 and SnO_2-1000). Commercial SnO_2 nanoparticles purchased from Sigma-Aldrich were used as comparison (Sigma Aldrich, SnO_2 nanopowder, ≤ 100 nm avg. part. size).

2.2 Characterization of SnO_2 nanoparticles

The synthesized nanoparticles were characterized on a carbon holey grid by TEM (JEOL, JEM-2010, Japan) for their morphology, and their size distribution was measured on the TEM images by ImageJ software on 50 particles per sample. The surface area was characterized by nitrogen adsorption and desorption isotherms at 150 °C (Autosorb-1, Quantachrome Instruments, US). The X-Ray diffraction was performed by an XRD D500/501 apparatus (Siemens, Berlin, Germany), equipped with Cu Ka radiation source from 10–80 2θ angle with 0.04 step. The crystallites size was determined according to Scherrer equation that relates the width of a powder diffraction peak to the average dimensions of crystallites in a polycrystalline powder:

$$D = K\lambda/\beta\ (2\theta)hkl\ \cos\theta,$$

where β is the crystallite size contribution to the peak width (full width at half maximum) in radians, K (shape factor) is a constant near unit and D is the average thickness of the crystal, in a direction normal to the diffracting plane hkl. The Raman analysis was carried out by an in Via Renishaw instrument with a laser of 514.5 nm at 5 mW.

SnO_2 particles morphology was also assessed by FESEM on a Zeiss SUPRA TM 40 with Gemini column and Schottky field emission tip (tungsten at 1800 K). Acquisitions were made at acceleration voltage of 3 kV and working distance (WD) between 2.1 and 8.5 mm, with magnification up to 150 KX.

2.3 SnO_2 anode preparation and half-cell assembling

All the electrodes were prepared by solvent tape casting method. Different slurries composed of SnO_2, conductive carbon additive (TIMCAL C-NERGYTM Super C65, Imerys Carb.) and a polymeric binder (poly(vinylidenedifluoride) PVdF-HSV900 dispersion at 10 wt.% in N-methyl-2-pyrrolidinone solution), in different weight ratio: (i) 40:50:10, (ii) 50:40:10, (iii) 60:30:10 and (iv) 70:20:10 were prepared in order to evaluate the effect of the mass-loading, and electrode composition. All the different mixtures were mechanically deposited on a copper current collector by Doctor Blade technique. The blade was adjusted for a 200 μm deposition using an automatic film applicator (Sheen 1133N) with a speed of 50 mm s^{-1}. Successively to the slurry deposition, the coated copper foil was dried at 60 °C for 1.5 hours in air. After solvent evaporation, disks of 0.785 and 1.766 cm^2 were punched out, vacuum dried at 120 °C (in a Büchi Glass Oven B-585) for 4 h, then transferred into an Argon filled dry glove-box (MBraun Labstar, H_2O and O_2 content < 1 ppm) for the half-cell and full-cell assembly. The final active material loading of the anode electrodes was respectively 1.1, 1.6, 2.5 and 3.5 mg cm^{-2} for (i), (ii), (iii) and (iv) respectively.

To evaluate the effect of the binder, slurries of SnO_2-400 (SnO_2 nanoparticles obtained from the 400 °C calcination), C65 and CMC in water, with weight ratio 70:20:10 (mass loading of 3.6 mg cm^{-2}) were prepared by the same procedure.

The as prepared electrodes were tested in 2032 coin cells (for galvanostatic cycling test), using lithium disks (Ø 16 mm, thickness 0.6 mm, Tobmachine) as counter and reference electrodes, while a glass-wool (glass fiber separator, thickness 0.65 mm, EL-Cell) was used as separator. The electrolyte adopted was a solution of 1.0 M $LiPF_6$ dissolved in a mixture 1:1 v/v of Ethylene Carbonate (EC) and Diethyl Carbonate (DEC) (battery grade, Solvionic).

The cycling performances were investigated by means of galvanostatic discharge-charge cycling (GC) using an Arbin BT-2000 battery tester at room temperature. GCs are carried out in the potential range of 0.01 – 2.0 V vs. Li/Li^+ at different C-rates (1495 mAh g^{-1} is the theoretical capacity of SnO_2). Here, the potential is referred versus Li/Li^+, and the specific charge is presented per mass of SnO_2 material.

To better evaluate the overall resistance inside the cells Potentiostatic Electrochemical Impedance Spectroscopy (PEIS) measurements were carried out by a versatile multichannel potentiostat (VMP-3 Biologic). Impedance measurements were performed using an amplitude of 10 mV in the frequency range of 500 kHz to 50 mHz.

Two-probe plane electronic conductivity measurement was used to evaluate the out-of-plane conductivity of the electrodes. Circular electrode discs with a diameter of 18 mm were inserted into EL cells ECC-Ref according to the following configuration: bottom cell – electrodes – current collector – pistons – spring – top cell. Galvanostatic Electrochemical Impedance Spectroscopy (GEIS) measurements were carried out by the multichannel potentiostat (VMP-3 Biologic). Impedance measurements were performed repeatedly on three different electrodes for each samples using an amplitude of 0.5 mA in the frequency range of 100 kHz to 100 mHz. During the GEIS measurements the working and counter electrodes were separated for the respective references in order to avoid the contribution of cable resistance.

2.4 LNMO cathode preparation and SnO_2/LNMO full cell assembly and characterization

The cathode slurry was prepared mixing 90 wt% of active material LNMO ($LiNi_{0.5}Mn_{1.5}O_4$, NANOMYTE-SP10, NEI corp.), 5 wt% of conducting Carbon Black (TIMCAL C-NERGYTM Super C65, ImerysCarb.) and 5 wt% of binder PVdF (HSV900, 10 wt.% in NMP solution) in N-methyl pyrrolidone. The as prepared slurry was casted on aluminium foil by a solvent tape casting method, using a doctor blade (adjusted for 300 μm deposition) and an automatic film applicator (Sheen 1133N) with a speed of 50 mm s^{-1}. After evaporating the solvent at 60 °C for 1.5 hours, electrode disks with an area of 1.766 cm^2 were punched out and vacuum dried at 120 °C (Büchi Glass Oven B-585) for 4 h, then transferred into an Argon filled dry glove-box (MBraum Labstar, H_2O and O_2 content < 1 ppm). The final mass loading of the LNMO dried electrodes was in the range of 6 mg cm^{-2}.

Before the full-cell assembly, the anode was charged and discharged ten times at C/10 with a final step of pre-lithiaion (at C/20) to 0.01 V in half-cell, in order to address the initial irreversible capacity loss and form a certain lithium reservoir. Subsequently, the anode electrode was coupled with LNMO electrode and tested either in T-cells (for three-electrodes test) or in coin cells 2032 (for two-electrodes test). The three-electrodes cell configuration was used to control and deconvolute the voltage profiles of the anode and cathode during charge and discharge process, using lithium metal as reference electrode. All electrochemical studies were performed at room temperature. The full cell electrochemical behaviour was investigated in two operational potential windows, from 3.5 – 4.9 V and 2.5 – 4.9 V vs. Li/Li^+. While the charge/discharge rate was based on the LNMO theoretical specific capacity of 147 mAh g^{-1}.

3 Results and Discussion

3.1 SnO_2 structural and morphological characterization

The first step of this study is aimed to screen the morphological and chemical-physical characteristics of the synthesized materials. In particular, the effect of the calcination treatment on the tin dioxide particles is evaluated.

Figure 1a-d shows the TEM and **Figure S1** the FESEM images of the sol-gel synthesized SnO_2 nanoparticles calcined at the different temperatures of 400°C, 700°C, 900°C, 1000°C respectively, and that of commercial SnO_2 is shown in **Figure S2b** as comparison. Both TEM and FESEM images indicate that SnO_2 is composed of nanoparticles that are in the order of five to fifty nanometres in size, depending on the calcination temperature. As can be seen in **Figure 1a, Figure S1a-b** and in **Figure S2a**, sample SnO_2-400 shows a homogeneous, uniform distribution of SnO_2 nanoparticles agglomerates. Moreover, SnO_2-400 nanoparticles appear ultra-fine, with a mean particle size of about 5.8 nm, which is very similar to the size of particles determined by XRD analysis using the Scherrer's equation, as shown in **Table S1**. For samples calcined above 400°C, the mean particle size of the nanoparticles, obtained by TEM analysis, increases with the calcination temperature (**Table S1**). This effect has been reported by Aziz *et al.* [42] who observed the same trend between the average particle size of SnO_2 and the calcination temperature. The structural coarsening of SnO_2 driven by temperature is attributed to the growth of nanometer-scale SnO_2 crystallites [35]. In fact, the microstructure at 700 °C and 1000 °C is similar but SnO_2-1000 has larger grain size and larger size distribution (**Figure 1b,c** and **Figure S1g-h**). Moreover, for samples SnO_2-700, SnO_2-900 and SnO_2-1000 a discrepancy is also observed between the mean particle

size obtained from TEM micrographs and the values calculated by the Scherrer's equation, indicating polycrystalline SnO_2 (**Table S1**).

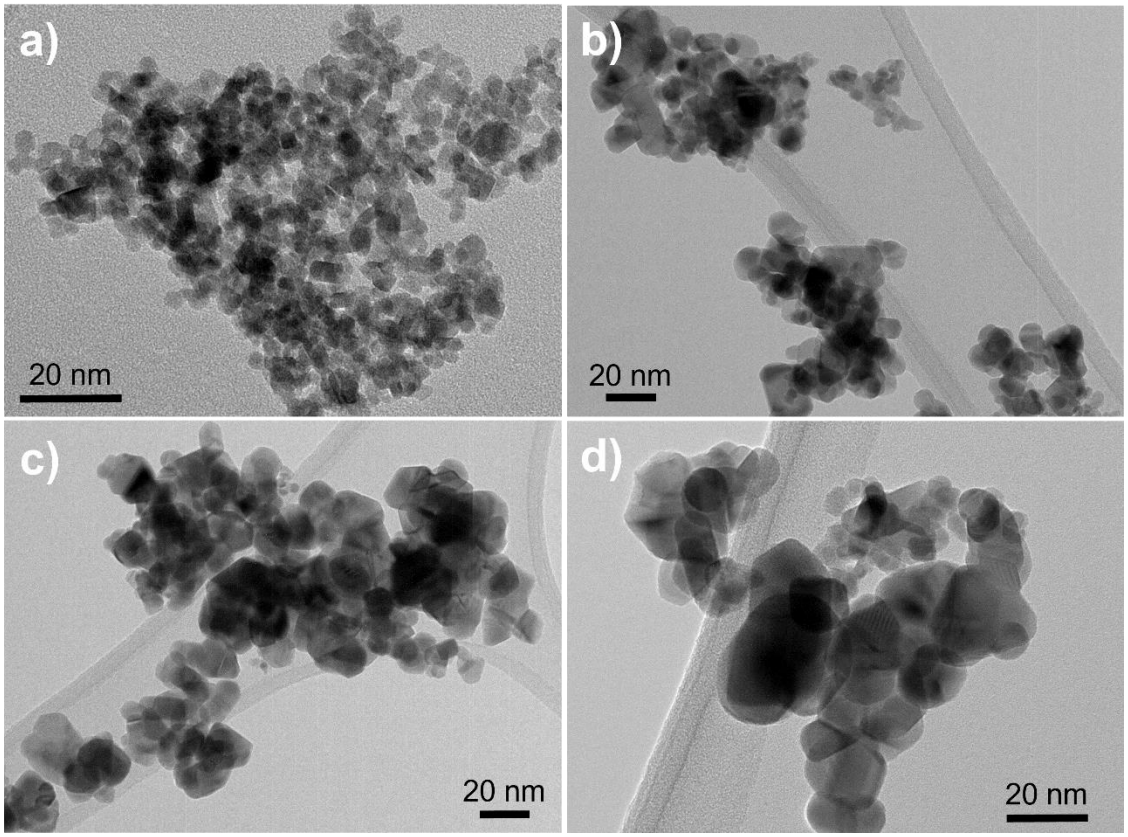

To evaluate the phase purity and the crystallite size of the synthesized SnO_2, XRD analysis is carried out and reported in **Figure 2a** with the XRD pattern of the commercial sample as comparison. The XRD analyses show the characteristic peaks of SnO_2 corresponding to the tetragonal rutile structure with a $P4_2/mnm$ space group (reference code 98-015-7448) and these results confirm a single phase. Among all the samples, SnO_2-400 exhibits broader peaks consistent to the smaller particle size and less degree of crystallinity. The XRD peaks of SnO_2 become sharp and narrow with the increase of the calcination temperature, this means that the phase does not change with temperature but the crystallinity degree increases as well as the nanoparticle size [43], as observed by TEM analysis. **Figure 2b** shows the Raman spectra of the synthesized SnO_2 nanoparticles. From Raman analysis the peaks at 633, 475 and 774 cm^{-1}, correspond to

the A_{1g}, E_g and B_{2g} vibrational modes, respectively. These are the typical modes of the tetragonal rutile structure of SnO_2 consistent to a pure phase sample [44]. In particular, A_{1g} and B_{2g} are attributed to the symmetric stretching modes of the Sn-O bond, while E_g is attributed to the vibration of oxygen in the oxygen plane. Additionally, two modes at 697 cm^{-1} and 543 cm^{-1} are exhibited in the Raman spectrum of SnO_2-1000 in **Figure 2b**, that are usually referred to local lattice disorder. In **Figure 2b**, the intensities of the A_{1g}, E_g and B_{2g} vibrational modes of SnO_2-400 are lower than those of the other SnO_2 samples and this can be related to the lower crystallinity degree and higher surface disorder of SnO_2-400. Finally, the blue shift of the A_{1g} mode further confirms the increase in particle size with the calcination temperature [44]. It is evident that the material calcined at the lower temperature 400 °C exhibits the highest surface area (88.6 m^2 g^{-1}), and the lowest crystallite size and particle size (5 nm), possibly due to monocrystalline nanoparticles; while further calcination increases particle and crystalline size and decreases surface areas, to values of 55 nm, 24 nm and 13 m^2 gr^{-1} respectively. The commercial material exhibits values in the range of 43 nm particle size, 36 nm crystallite size and 8 m^2 gr^{-1} surface area.

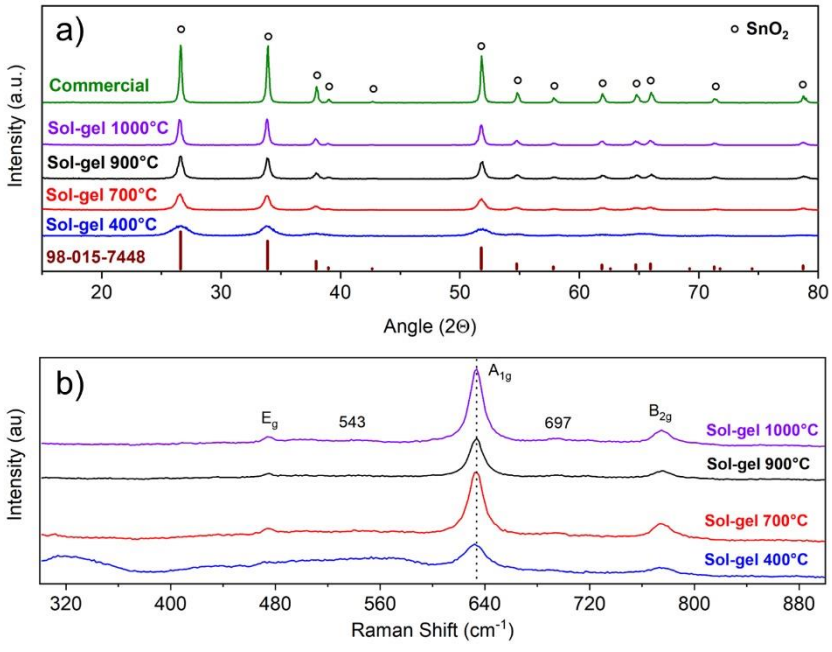

In relation to previous studies [45] it is expected that nanosized SnO_2 shows advantages in cycling behaviour with characteristics related to strong resistance to fragmentation, less volumetric changes during conversion/alloying reactions and enhanced diffusion of Li-ions in the bulk phase. Thus, the attention has been focused on the sol-gel monocrystalline SnO_2-400 material with the smallest particle size (5 nm) and larger BET surface area which is expected to show enhanced electrochemical performance.

3.2 Electrochemical characterization

3.2.2 Characterization of SnO_2-400 half cell tests: the effect of the mass loading.

As mentioned before, in addition to morphology, the electrochemical performance of SnO_2 is highly sensible to the electrode composition [46]. In this section, SnO_2-400 sample is selected and the effect of electrode engineering, such as the mass loading, is analysed. For this reason, four electrodes are prepared with different weight ratio of active and inactive components (named: SnO_2-400-40%, SnO_2-400-50%, SnO_2-400-60%, SnO_2-400-70%), corresponding to active material loadings of 1.15, 1.61, 2.55 and 3.65 mg cm^{-2}, respectively. Galvanostatic cycling is performed in half cells to assess the electrochemical performances of the different electrodes. After three cycles at C/10, the cells are galvanostatically lithiated at 1C for 100 cycles and then at C/10 for the last three cycles, within the potential range of 0.01 – 2.0 V. Delithiation is performed at 1C. **Figure 3a-d** show the specific capacity vs cycle number for SnO_2-400 cells with different SnO_2 mass loadings. As can be seen at the 2^{nd} cycle at C/10, all cells experience similar lithiation capacity, which ranges between 984 and 1154 mAh g^{-1} depending on the SnO_2

mass loading, reaching 66 – 77% of the total theoretical capacity of the material. **Figure 3a** shows that SnO_2-400-40% cell delivers stable capacity of 550 mAh g^{-1} at 1C and retains 660 mAh g^{-1} at C/10 after 100 cycles. Similarly, the electrode containing 50% of SnO_2 shows a capacity retention higher than 50% at 1C and a specific capacity close to 650 mAh g^{-1} at C/10 after 100 cycles. On the contrary, the electrodes with higher mass loadings experience lower capacity retention at 1C, which is 33% for SnO_2-400-60% and 23% for SnO_2-400-70%, calculated from the 4th to the 103rd cycle. From these results, there is a clear evidence of the benefit of carbon black addition to SnO_2-400 in the electrode preparation, which improves the electrochemical performances at higher C-rates (1C).

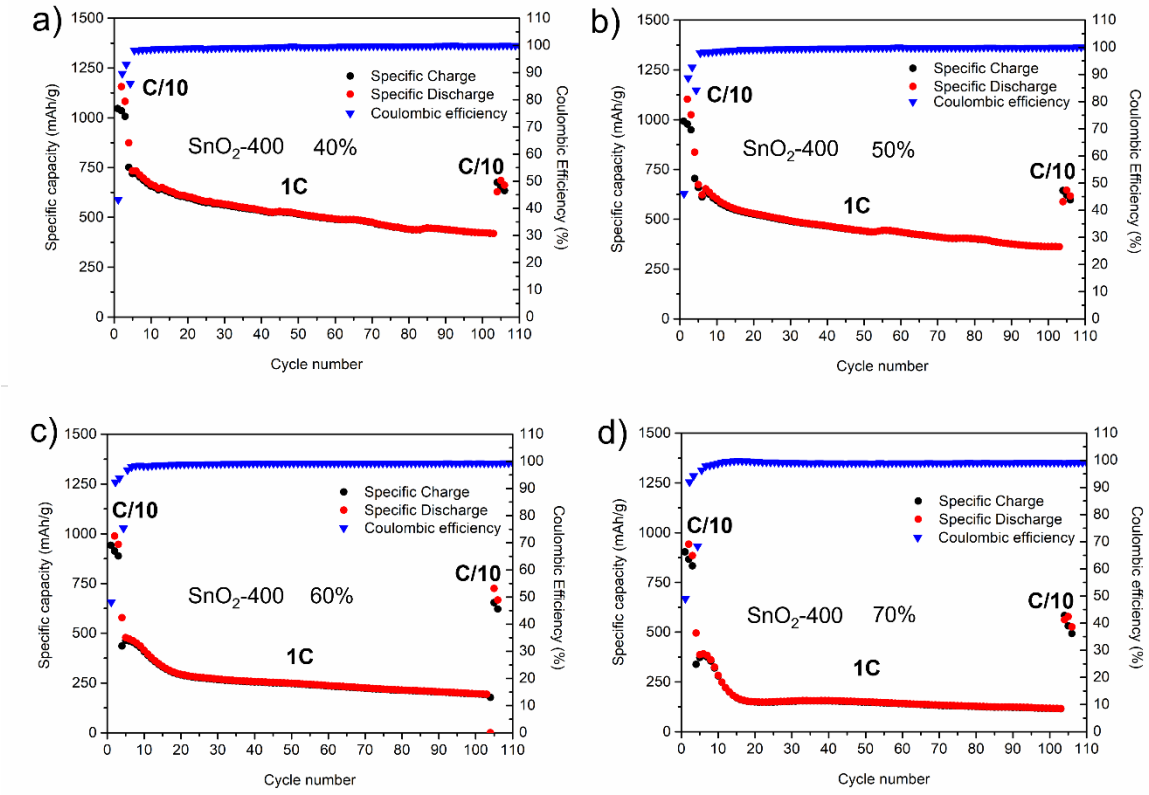

In **Figure S4a-g** the specific capacity vs voltage plots at the 1st, 2nd and 105th cycle at C/10 of SnO_2-400 are reported, along with the corresponding differential capacity vs voltage curves. The differential capacity plots are smooth and display fewer sharp peaks.

This trend is typical of small grain and less crystalline SnO_2 material [47]. The overall voltage profile at the 1st cycle at C/10 (**Figure S4a**) leads to high irreversible capacity (2500 mAh g^{-1}) during initial lithiation, consistent with more severe electrolyte decomposition and higher solid electrolyte interface (SEI) formation, due to the high specific surface area of SnO_2-400 [48]. The differential capacity profiles (**Figure S4d, e**) show additional peaks at 0.03V (in reduction) and at 0.07 V (in oxidation). These peaks disappear in the dQ/dV plots when the weight percentage of C in the electrode is decreased, and can be related to the intercalation of Li ions into carbon black. This accounts for a small fraction of the total capacity delivered by SnO_2-400 (SnO_2 40% and SnO_2 50%) along with the larger irreversible capacity observed at the 1st cycle. Differential capacity profiles at the 105th cycle (green line in **Figure S4d-f**) show the role of carbon black in limiting aggregation of Sn during cycling. In fact, the peaks related to the conversion and alloying reactions of SnO_2 are clearly visible in the dQ/dV curves of the electrodes with higher C content (SnO_2 40% and SnO_2 50%). At the 105th cycle, large and smooth peaks appear in the dQ/dV curves of SnO_2 70%, this shape is associated with the aggregation of Sn into larger regions during cycling [45]. These results highlight that at least 40% of C in the electrode composition is necessary, both to increase the conductivity and prevent coalescence of tin particles.

In order to understand the role of carbon black in the electrode formulation, two-probe plane measurements have been carried out to study the conductivity of electrodes, in particular the out-of-plane conductivity, which controls the charge transport from the current collector to the active sites [49]. The experimental set-up is reported in **Figure S4**. Basically, Galvanostatic Electrochemical Impedance Spectroscopy (GEIS) is used to measure the resistance (R) that is the sum of the resistance of the composite material (SnO_2/Carbon black/binder) and the contact resistance. This resistance can be used to

calculate the resistivity (ρ) of the system and the conductivity (σ), according to equation (1) and (2) reported in the SI.

As can be seen in **Table S2**, similar values of conductivity are obtained for the electrodes containing 40 and 50 wt.% of SnO_2, respectively. The electronic conductivity increases for the electrode with 60 wt.% of SnO_2 and decreases again by increasing SnO_2 content to 70 wt.%. These values highlight that the electronic conductivity is not simply related to content of carbon black in the electrode but is the result the complex distribution of the materials inside the electrode along with the formation of conductive networks with different porosity and tortuosity. In fact, the higher electronic conductivity does not directly correspond to the higher capacity values, since also the ionic conductivity plays a fundamental role both at high and low C-rates [50].

To better evaluate the overall cell resistance, Potentiostatic Electrochemical Impedance Spectroscopy (PEIS) analysis was performed during the forming cycles for all the electrodes more precisely, at the end of the first and the third cycle at C/10. As reported in **Figure S5a,b**, the Nyquist plots show two semicircles: one at high frequencies referring to SEI layer resistance (R_{SEI}) and the second at mid-frequencies related to charge transfer resistance (R_{CT}). The initial resistance at the highest frequencies is due to the electrolyte resistance and/or contact resistance (R_{EL}), while the straight line at low frequencies represents the lithium-ion diffusion in the bulk material [51]. All Nyquist plots are fitted according to the equivalent circuit reported in **Figure S5c** and the fitted values are listed in **Table S3**. From the Nyquist plot, the cells show very low resistance, which is lower than 20 Ω. From fitting the Nyquist profiles, it is possible to identify and discriminate the various contributions of the resistance. The initial resistance (R_{EL}) is between 4 and 6 Ω and lower for the electrodes with higher amounts of carbon black. This could be related

to the higher permeation of the electrolyte in the porosity of the electrode and to the lower contact resistance. However, at the third cycle, R_{EL} remains roughly constant for SnO_2-400-50, SnO_2-400-60 and SnO_2-400-70, while it increases for SnO_2-400-40. This is probably due to a greater reactivity of the carbon black with the electrolyte. The greater tendency to form SEI layer at the electrolyte/electrode interface with higher amount of carbon black is confirmed by the R_{SEI} observed after the first cycle, which turns out to be higher for SnO_2-400-40 than for the others. The charge transfer resistance (R_{CT}) decreases as the amount of SnO_2 increases. This should be due to the better distribution of the components within the electrode, which facilitates the charge transfer from one particle to another. However, all R_{CT} values are very similar and in the range of 5.5 to 8.9 Ω. After three cycles, both the R_{SEI} and the R_{CT} decrease, confirming that more stable SEI layer is achieved. To sum up, the internal resistance of the different electrodes is similar. However, after several cycles, the cell capacity is strongly influenced by the initial distribution of both SnO_2 and carbon particles inside the electrode, since such distribution allows the carbon particles to better buffer the volume changes of SnO_2.

3.2.2 Characterization of SnO_2-400 half cell tests: the effect of binder.

Equally to the mass loading optimization, the use of less expensive binders and eco-sustainable processes turns out to be one of the most important challenges of future electrode manufacturing process [52]. In this frame, commercial sodium carboxymethyl cellulose (Na-CMC), containing carboxylic groups acting as dispersing agents during slurry preparation [46], should feature many advantages over PVdF binder, especially with ultra-fine SnO_2 nanoparticles [53]. To verify such hypothesis, the composition

70:20:10 (SnO_2-400:C45:CMC), corresponding to the highest mass loading obtained in the previous part, has been selected.

This formulation was selected because it is the most extreme condition, in terms of amount of SnO_2, reported in this study. In fact, As can be seen in the previous paragraph, the higher amount of SnO_2 in the electrode corresponds to the lower specific capacity and capacity retention. At the same time, high SnO_2 mass loadings allow to better appreciate the role of the binder and its influence on the electrochemical properties of the electrode.

The galvanostatic charge/discharge performance with CMC are shown in **Figure 4a** against those of SnO_2-400 electrode with similar mass loading (3.65 mg cm^{-2}) and PVDF binder. With water-based binder SnO_2-400 has twice the capacity, with the same number of cycles, and affords better capacity retention compared to PVDF. These results highlight that CMC offers better connectivity between SnO_2-400 and carbon black particles, allowing higher SnO_2 utilization than PVDF, at comparable mass loading. **Figure 4b-c** shows the voltage profile and dQ/dV plots of SnO_2 anodes with the different binders at the 1^{st} cycle. The shape of the dQ/dV plot at the 1^{st} cycle is different for the two binders, suggesting different interfacial reactions. Two peaks at 2.35 and 1.4 V (highlighted with black arrows in **Figure 4c**) can be seen with SnO_2-PVDF electrode, which are mostly ascribable to the reduction of the electrolyte [54]. These peaks are not present in the dQ/dV of SnO_2-CMC, which exhibits only a small peak at 1.2 V. A similar behaviour was observed on Si anodes by Lucht and co-workers [55], who reported the formation of a thick SEI layer after 5 charge/discharge cycles with PVDF binder. They claimed that the SEI isolated the Si NPs and was responsible for a rapid capacity decay. On the contrary, a thinner SEI was observed around Si NPs when using CMC, which resulted in better cyclability. This might explain the higher specific capacity (349 mAh g^{-1} for SnO_2/CMC vs 149 mAh g^{-1} for SnO_2/PVDF at 50^{th} cycle, 1C) and the better capacity

retention (36.24% for SnO_2/CMC vs 31.2% for SnO_2/PVDF after 100 cycles at 1C) observed for SnO_2-400 with CMC binder.

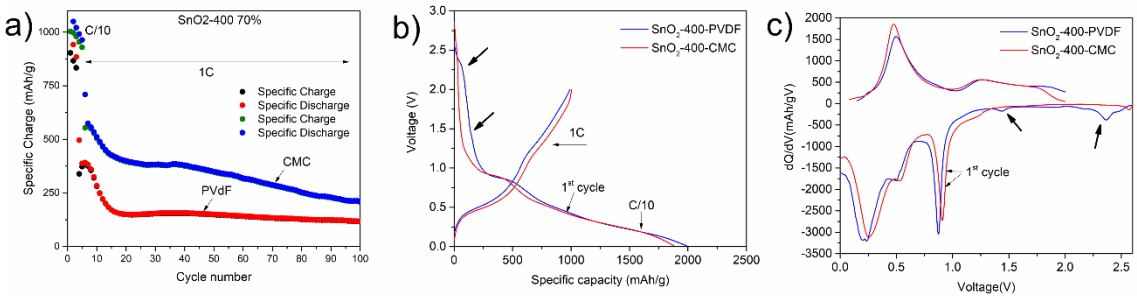

To sum up, the CMC binder, which is rich of acidic functionalities, can better interact with tin oxide nanoparticles, by hydrogen and/or covalent bonding, allowing an enhancement of electrode performances even at the highest SnO_2 mass loadings that can be achieved with the coin cell design.

3.2.3 Characterization of the SnO_2-400/LNMO Li-ion full cell.

In order to study the behaviour of SnO_2-400 as alternative anode to graphite in a full Li-ion cell, the SnO_2 anode is tested against a commercial LNMO cathode.

Starting from the observations of the previous paragraphs, an anode composition of 50 %wt of SnO_2-400 is selected, as good compromise in terms of mass loading and electrochemical performances. At the same time, CMC is chosen as aqueous binder for its higher electrochemical stability, eco-sustainability and reduced cost. While for the cathode composition, the selected ratio is 90:5:5 (LNMO:C65:PVdF).

For the electrochemical characterization, two different cell designs are used: three-electrodes T-cell and 2-electrodes coin-cell configuration. In fact, T-cell configuration

446 enables the use of a Li reference electrode for monitoring the potential of individual
447 electrodes, while the coin cell design enables longer cycling tests at C/10.

448 Prior to cell assembly, both SnO_2 and LNMO are individually cycled vs. Li anode in
449 the half coin cell configuration, mainly to limit the large irreversibility of SnO_2 anode and
450 build up a certain Li reservoir. Specifically, the procedure for SnO_2 involves 10 cycles at
451 C/10 followed by one lithiation at C/20 until the cut-off potential of 0.01 V is reached.
452 The N:P ratio, was calculated on the basis of the practical capacities of both electrodes,
453 obtained at C/10 in half-cell configuration, and it has been set to a value of ~1.1/1.2. In
454 the full-cell the dis-/charge rate is based on the LNMO cathode at C/10, which
455 corresponds to a specific current of 14.5 mA g^{-1} LNMO. Two operational potential
456 windows of 2.5 – 4.9 V and 3.5 – 4.9 V are selected for cycling the full cell, in order to
457 better understand and exploit the electrochemical behaviour of the electrodes. As
458 depicted in **Figure S6a,c** the full cell with SnO_2/LNMO cycled in the potential range of
459 2.5 – 4.9 V shows an initial discharge capacity of 100 mAh g–1 based on the sum of the
460 masses of the negative and positive active materials, which corresponds to 118 mAh g–1
461 based on the LNMO active mass only. The initial Coulombic efficiency is around 89% at
462 the 1st cycle and then settles to 97% until the 50th cycle is reached. Considering and
463 average voltage of 4.2 V, the specific energy (based on the anode and cathode active
464 material) is higher than 400 Wh kg^{-1} for more than 15 cycles. As can be seen in **Figure**
465 **S6a**, after the first cycles the cell experiences a slight but steady capacity fading. This
466 observation can be clarified by considering the voltage characteristics of both electrodes
467 in **Figure S6c**, which depicts the trend of the potential vs time of the full cell, the anode
468 and the cathode, respectively. In fact, cycling the full cell in the potential range 2.5 – 4.9
469 V, the anode reaches the upper cut-off voltage of 1.06 V while the lower cut-off voltage

is 0.2 V, which means that, in this regime of potential, both the conversion and the alloying reactions of SnO_2 are not fully exploited. At the same time, for LNMO the lower cut-off voltage is 4.7 V, which implies that only the two-nickel redox couple are involved in the reaction while the manganese couple remains unutilized. This results in 55% capacity retention from the 1st to the 50th cycle. On the other hand, when decreasing the potentials in the range 3.5 – 4.9 V, the SnO_2/LNMO full cell shows a very stable specific capacity for the first 12 cycles (**Figure 5a**). Also in this case, the initial Coulombic efficiency is rather low, around 87%, which indicates a certain fraction of side reactions due to SEI formation, but then it stabilizes at 97% until the 50th cycle. Concerning the specific capacity, at the 2nd cycle, it is 105 mAh g^{-1} based on the total mass of active material, corresponding to 127 mAh g^{-1} considering only LNMO mass, which means that the full capacity of the cathode is used.

As depicted in **Figure 5c**, within this cell cut-off potentials (between 3.5 and 4.9 V) the LNMO cathode experiences stable dis-/charge cycles, and both the manganese (at 4.1 V vs Li/Li^+) and the nickel (at 4.7 V vs Li/Li^+) redox couples are clearly visible, in particular in the early cycles. In addition, at the 1st cycle, SnO_2 operates within the range of potential of 0.96 – 0.01 V vs Li/Li^+, which means that the anode does not reach its upper cut-off voltage and the conversion reaction does not take place at full capacity. However, a slight increase of the upper cut-off voltage of the anode is observed in the following cycles (**Figure 5c**), which becomes more and more important as the number of cycles increases until the upper cut-off voltage of 2.0 V is reached (**Figure 5d**). The mentioned shift of the anode potential is accompanied with the capacity loss of the full cell during the first 20 cycles (**Figure 5a**), and the fading of the redox plateau of the manganese couple of the LNMO cathode, which disappears at around the 7th cycle (**Figure 5d**). This phenomenon has been explained as a loss of electrochemically available lithium [56], which is

consumed in continuous SEI formation. It is important to note that, apart from the electrolyte, lithium mainly comes from the LNMO material, which continuously experiences Li^+ losses in the full cell during cycling, compared to its behaviour in the half-cell (*i.e.* vs lithium) [57][58].

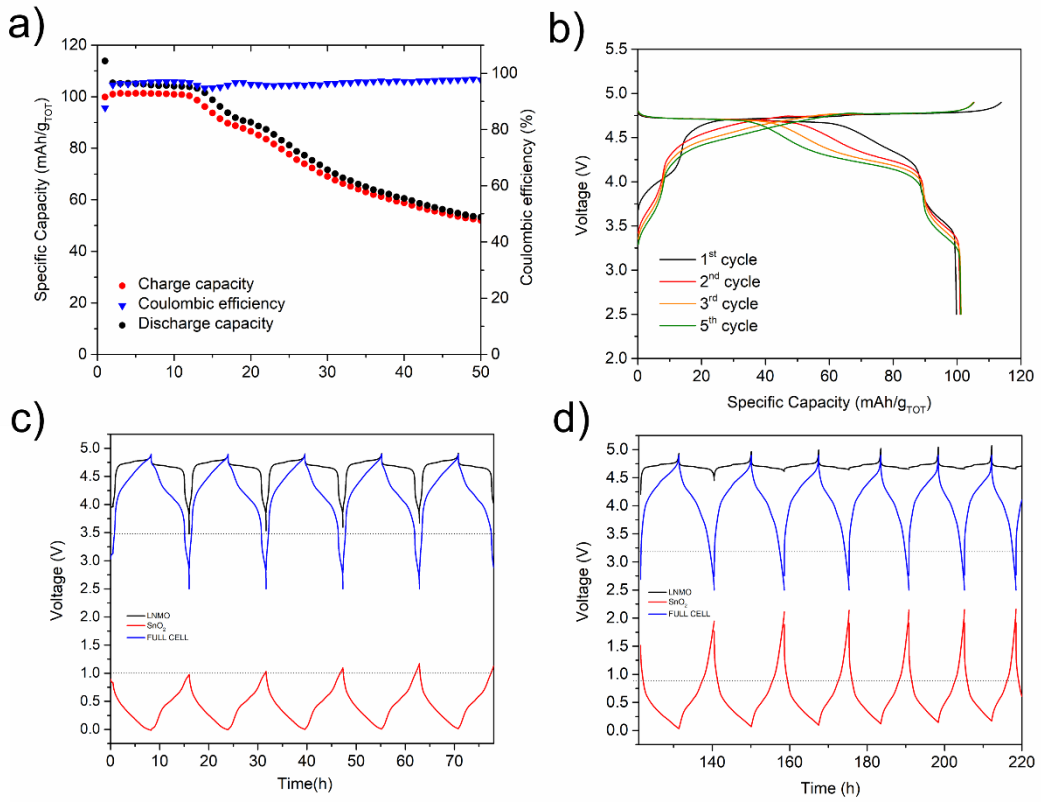

To better highlight the single electrode behaviour in 2-electrodes full cell, the differential capacity vs voltage plots (dQ/dV) of the LNMO cathode, vs Li reference electrode at the 1st and 15th cycle, are shown in **Figure S7**. At the 1st cycle, the peaks of Ni $^{II/III}$ oxidation at the potential of 4.70 V and the Ni $^{III/IV}$ oxidation at 4.74 V are clearly seen, meaning that the lithium amount is enough for the complete lithiation of the LNMO material. After 15 cycles, there is a shift of the oxidation peaks of nickel towards lower potentials, which is accompanied by the decreasing of Ni $^{II/III}$ peak and by the increasing of the Ni $^{III/IV}$ peak. As cycling proceeds, the fraction of fully lithiated phase, which corresponds to the Ni $^{III/IV}$ couple, also decreases because the electrochemically available

lithium in the cell is bound at the electrode [56], this explains the observed capacity fading from the 15th to the 50th cycle in the full cell, observed in **Figure 5a**.

In order to verify that the loss of electrochemically available lithium is mainly responsible for the degradation of the capacity in the full cell, both the cathode and the anode were retrieved from the full cell and two half-cells were assembled with Li as counter electrode. **Figure 6a** shows the capacity voltage curves of the LNMO cathode after cycling in the full cell compared to those of pristine LNMO (**Figure 6b**). Except for the 1st cycle, in which the capacity of the cathode is still affected by the incomplete lithiation of LNMO experienced in the full cell (which corresponds to a charge capacity of 51 mAh g^{-1}), then the capacity settles down to the value of 120 mAh g^{-1}, which is comparable to the one obtained with the pristine LNMO cathode (128 mAh g^{-1}). This behaviour is maintained in the following cycles (**Figure 6c**) indicating no substantial modifications in the LNMO material after cycling in the full cell. A similar behaviour is observed for SnO_2-400 (**Figure 6d**), except for a capacity loss of 23% with respect to the pristine material (**Figure 6e**). The trend of capacity of the recovered SnO_2 anode in the half cell is fully consistent with its capacity retention with cycling, which is depicted in **Figure 3**.

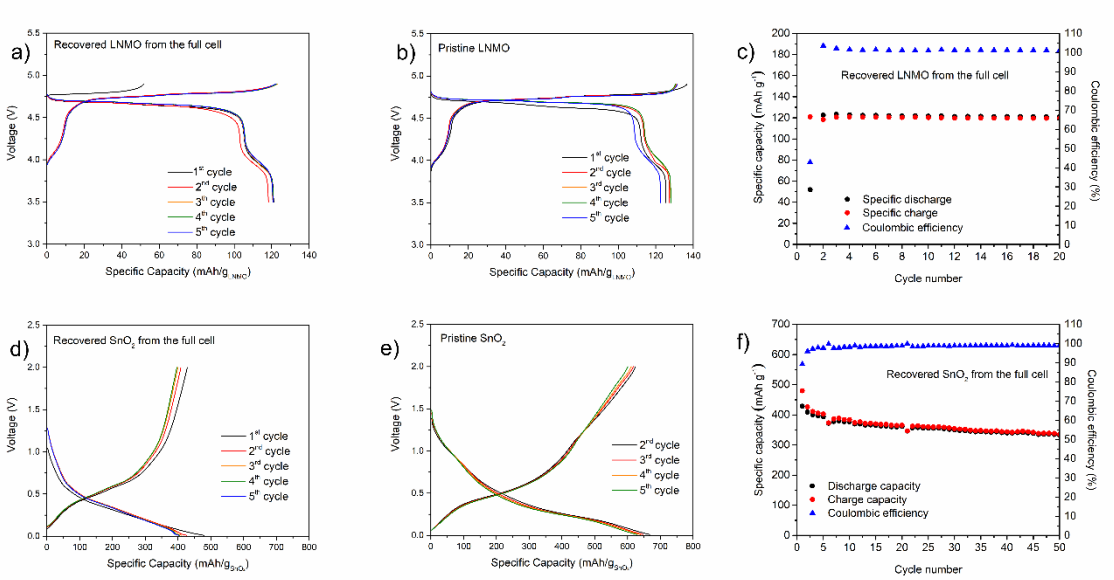

527

528

529 In general, the obtained performances are in line with similar systems based on
530 conversion/alloying anodes and LNMO cathodes [59],[60]. The cycling stability of the
531 cell is comparable to full cells based on TiO_2 coated-SnO_2 anodes and LFP cathodes [61],
532 and only slightly lower than that of chemically pre-lithiated nanocomposite SnO_2/C
533 electrodes [62] and TM co-doped SnO_2 with N/P ratio of 2 [60]. Nevertheless, a direct
534 comparison is not simple, because most of the works use different cathode materials in
535 combination with the SnO_2 anode, which imply that different potential ranges, SnO_2 mass
536 loadings and electrolytes are used. In this work, the capacity of the full cell, in the
537 potential range of 3.5 – 4.9 V, is greater than 350 mAh g^{-1} at the 50^{th} cycle, which is
538 consistent with the values reported in literature, where SnO_2 is combined with other
539 cathode materials (NMC, LFP, etc) [63–70]. In addition, it is worth noting that, in the
540 present work, except for the SnO_2 particles size optimization, no further strategies have
541 been adopted (*i.e.* electrolyte optimization, carbon coating, chemical pre-lithiation or

other complex approaches [71]), which would have been useful to improve the cycling stability.

4 Conclusions

A scalable sol-gel method was proved to be suitable to synthesise phase-pure and crystalline SnO_2 and finely dispersed nanoparticles with and average size of about 5 nm, which can be controlled by optimizing the calcination temperature at 400 °C. The additional optimization of the electrode composition further improved the cycling stability and SnO_2-400 exhibited a reversible specific capacity higher than 350 mAh g^{-1}, with a coulombic efficiency close to 99.9 % after 100 cycles, adopting a higher current regime of 0.75 A g^{-1}. The optimized SnO_2 electrode was then pre-lithiated and coupled with a LNMO-based cathode showing high energy density of about 400 Wh kg^{-1}, corresponding to a reversible specific capacity higher than 350 mAh g^{-1} (based on the SnO_2 mass) which makes the combination of these two electrodes an interesting option for the next generation Li-ion batteries. Overall, this study has revealed that the investigation of the electrode formulation, beneficial to increase both the electrochemical characteristics (electronic conductivity, reversibility of processes, coulombic efficiency, etc.), and the mechanical properties (particle distribution, adhesion between components, cycling stability) along with the identification of the best conditions for electrochemical testing, have a dramatic impact on the performance of full cells, and it is expected to provide some guidelines for the development of future tin oxide-based advanced anodes.

References

[1] M. Fichtner, K. Edström, E. Ayerbe, M. Berecibar, A. Bhowmik, I.E. Castelli, S. Clark, R. Dominko, M. Erakca, A.A. Franco, A. Grimaud, B. Horstmann, A. Latz, H. Lorrmann, M. Meeus, R. Narayan, F. Pammer, J. Ruhland, H. Stein, T. Vegge, M. Weil, Rechargeable Batteries of the Future—The State of the Art from a BATTERY 2030+ Perspective, Adv Energy Mater. 12 (2022). https://doi.org/10.1002/aenm.202102904.

[2] J. Amici, P. Asinari, E. Ayerbe, P. Barboux, P. Bayle-Guillemaud, R.J. Behm, M. Berecibar, E. Berg, A. Bhowmik, S. Bodoardo, I.E. Castelli, I. Cekic-Laskovic, R. Christensen, S. Clark, R. Diehm, R. Dominko, M. Fichtner, A.A. Franco, A. Grimaud, N. Guillet, M. Hahlin, S. Hartmann, V. Heiries, K. Hermansson, A. Heuer, S. Jana, L. Jabbour, J. Kallo, A. Latz, H. Lorrmann, O.M. Løvvik, S. Lyonnard, M. Meeus, E. Paillard, S. Perraud, T. Placke, C. Punckt, O. Raccurt, J. Ruhland, E. Sheridan, H. Stein, J.-M. Tarascon, V. Trapp, T. Vegge, M. Weil, W. Wenzel, M. Winter, A. Wolf, K. Edström, A Roadmap for Transforming Research to Invent the Batteries of the Future Designed within the European Large Scale Research Initiative BATTERY 2030+, Adv Energy Mater. 12 (2022). https://doi.org/10.1002/aenm.202102785.

[3] B. Babu, P. Simon, A. Balducci, Fast Charging Materials for High Power Applications, Adv Energy Mater. 10 (2020). https://doi.org/10.1002/aenm.202001128.

[4] M. Weiss, R. Ruess, J. Kasnatscheew, Y. Levartovsky, N.R. Levy, P. Minnmann, L. Stolz, T. Waldmann, M. Wohlfahrt-Mehrens, D. Aurbach, M. Winter, Y. Ein-Eli, J. Janek, Fast Charging of Lithium-Ion Batteries: A Review of Materials Aspects, Adv Energy Mater. 11 (2021). https://doi.org/10.1002/aenm.202101126.

[5] J. Asenbauer, T. Eisenmann, M. Kuenzel, A. Kazzazi, Z. Chen, D. Bresser, The success story of graphite as a lithium-ion anode material-fundamentals, remaining challenges, and recent developments including silicon (oxide) composites, Sustain Energy Fuels. 4 (2020) 5387–5416. https://doi.org/10.1039/d0se00175a.

[6] H. Zhang, Y. Yang, D. Ren, L. Wang, X. He, Graphite as anode materials: Fundamental mechanism, recent progress and advances, Energy Storage Mater. 36 (2021) 147–170. https://doi.org/10.1016/j.ensm.2020.12.027.

[7] M. Armand, P. Axmann, D. Bresser, M. Copley, K. Edström, C. Ekberg, D. Guyomard, B. Lestriez, P. Novák, M. Petranikova, W. Porcher, S. Trabesinger, M. Wohlfahrt-Mehrens, H. Zhang, Lithium-ion batteries – Current state of the art and anticipated developments, J Power Sources. 479 (2020). https://doi.org/10.1016/j.jpowsour.2020.228708.

[8] H. Cheng, J.G. Shapter, Y. Li, G. Gao, Recent progress of advanced anode materials of lithium-ion batteries, Journal of Energy Chemistry. 57 (2021) 451–468. https://doi.org/10.1016/j.jechem.2020.08.056.

[9] M.A. Azam, N.E. Safie, A.S. Ahmad, N.A. Yuza, N.S.A. Zulkifli, Recent advances of silicon, carbon composites and tin oxide as new anode materials for lithium-ion battery: A

comprehensive review, J Energy Storage. 33 (2021). https://doi.org/10.1016/j.est.2020.102096.

[10] L. Sun, Y. Liu, R. Shao, J. Wu, R. Jiang, Z. Jin, Recent progress and future perspective on practical silicon anode-based lithium ion batteries, Energy Storage Mater. 46 (2022) 482–502. https://doi.org/10.1016/j.ensm.2022.01.042.

[11] M. Ge, C. Cao, G.M. Biesold, C.D. Sewell, S.-M. Hao, J. Huang, W. Zhang, Y. Lai, Z. Lin, Recent Advances in Silicon-Based Electrodes: From Fundamental Research toward Practical Applications, Advanced Materials. 33 (2021). https://doi.org/10.1002/adma.202004577.

[12] S. Bobba, S. Carrara, J. Huisman, F. Mathieux, C. Pavel, Critical Raw Materials for Strategic Technologies and Sectors in the EU - a Foresight Study, 2020. https://doi.org/10.2873/58081.

[13] P. Meister, H. Jia, J. Li, R. Kloepsch, M. Winter, T. Placke, Best Practice: Performance and Cost Evaluation of Lithium Ion Battery Active Materials with Special Emphasis on Energy Efficiency, Chemistry of Materials. 28 (2016) 7203–7217. https://doi.org/10.1021/acs.chemmater.6b02895.

[14] X. Lan, X. Xiong, J. Liu, B. Yuan, R. Hu, M. Zhu, Insight into Reversible Conversion Reactions in SnO2-Based Anodes for Lithium Storage: A Review, Small. 18 (2022). https://doi.org/10.1002/smll.202201110.

[15] F. Zoller, D. Böhm, T. Bein, D. Fattakhova-Rohlfing, Tin Oxide Based Nanomaterials and Their Application as Anodes in Lithium-Ion Batteries and Beyond, ChemSusChem. 12 (2019) 4140–4159. https://doi.org/10.1002/cssc.201901487.

[16] S. Wang, G. Xu, K. Wang, B. Han, Y. Wang, L. Li, D. Ju, M. Chai, D. Zhang, W. Zhou, Fabrication and electrochemical performances of SnO2@C composite materials, Current Research in Green and Sustainable Chemistry. 4 (2021). https://doi.org/10.1016/j.crgsc.2021.100099.

[17] D. Versaci, A. Costanzo, S.M. Ronchetti, B. Onida, J. Amici, C. Francia, S. Bodoardo, Ultrasmall SnO2 directly grown on commercial C45 carbon as lithium-ion battery anodes for long cycling performance, Electrochim Acta. 367 (2021). https://doi.org/10.1016/j.electacta.2020.137489.

[18] D. Versaci, J. Amici, C. Francia, S. Bodoardo, Simple approach using g-C3N4 to enable SnO2 anode high rate performance for Li ion battery, Solid State Ion. 346 (2020). https://doi.org/10.1016/j.ssi.2019.115210.

[19] R. Liu, W. Su, P. He, C. Shen, C. Zhang, F. Su, C.-A. Wang, Synthesis of SnO2/Sn hybrid hollow spheres as high performance anode materials for lithium ion battery, J Alloys Compd. 688 (2016) 908–913. https://doi.org/10.1016/j.jallcom.2016.07.194.

[20] J.S. Chen, L.A. Archer, X. Wen Lou, SnO2 hollow structures and TiO2 nanosheets for lithium-ion batteries, J Mater Chem. 21 (2011) 9912–9924. https://doi.org/10.1039/c0jm04163g.

[21] R. Liu, W. Su, C. Shen, J. Iocozzia, S. Zhao, K. Yuan, N. Zhang, C.-A. Wang, Z. Lin, Hydrothermal synthesis of hollow SnO2 spheres with excellent electrochemical performance for anodes in lithium ion batteries, Mater Res Bull. 96 (2017) 443–448. https://doi.org/10.1016/j.materresbull.2017.03.004.

[22] Y. Li, J. Song, X. Hong, Q. Tian, Z. Sui, L. Yang, Boosting the lithium storage performance of tin dioxide by carbon nanotubes supporting and surface engineering, J Colloid Interface Sci. 602 (2021) 789–798. https://doi.org/10.1016/j.jcis.2021.06.076.

[23] G.-L. Xu, Y.-D. Gong, C. Miao, Q. Wang, S.-Q. Nie, Y. Xin, M.-Y. Wen, J. Liu, W. Xiao, Sn nanoparticles embedded into porous hydrogel-derived pyrolytic carbon as composite anode materials for lithium-ion batteries, Rare Metals. 41 (2022) 3421–3431. https://doi.org/10.1007/s12598-022-02073-3.

[24] Q. Tian, Y. Chen, Z. Sui, J. Chen, L. Yang, The sandwiched buffer zone enables porous SnO2@C micro-/nanospheres to toward high-performance lithium-ion battery anodes, Electrochim Acta. 354 (2020). https://doi.org/10.1016/j.electacta.2020.136699.

[25] C.-P. Wu, K.-X. Xie, J.-P. He, Q.-P. Wang, J.-M. Ma, S. Yang, Q.-H. Wang, SnO2 quantum dots modified N-doped carbon as high-performance anode for lithium ion batteries by enhanced pseudocapacitance, Rare Metals. 40 (2021) 48–56. https://doi.org/10.1007/s12598-020-01623-x.

[26] J.Y. Huang, L. Zhong, C.M. Wang, J.P. Sullivan, W. Xu, L.Q. Zhang, S.X. Mao, N.S. Hudak, X.H. Liu, A. Subramanian, H. Fan, L. Qi, A. Kushima, J. Li, In situ observation of the electrochemical lithiation of a single SnO 2 nanowire electrode, Science (1979). 330 (2010) 1515–1520. https://doi.org/10.1126/science.1195628.

[27] M. Mirolo, X. Wu, C. A. F. Vaz, P. Novák, M. El Kazzi, Elucidation of the Complex (De-)Lithiation Reactions of SnO 2 in All Solid-State Battery Using Operando X-Ray Photoelectron Spectroscopy, ECS Meeting Abstracts. MA2019-02 (2019) 708–708. https://doi.org/10.1149/MA2019-02/7/708.

[28] S. Zhao, C.D. Sewell, R. Liu, S. Jia, Z. Wang, Y. He, K. Yuan, H. Jin, S. Wang, X. Liu, Z. Lin, SnO2 as Advanced Anode of Alkali-Ion Batteries: Inhibiting Sn Coarsening by Crafting Robust Physical Barriers, Void Boundaries, and Heterophase Interfaces for Superior Electrochemical Reaction Reversibility, Adv Energy Mater. 10 (2020). https://doi.org/10.1002/aenm.201902657.

[29] D. Zhou, W.L. Song, L.Z. Fan, Hollow Core-Shell SnO2/C Fibers as Highly Stable Anodes for Lithium-Ion Batteries, ACS Appl Mater Interfaces. 7 (2015) 21472–21478. https://doi.org/10.1021/acsami.5b06512.

[30] Q. Tan, Z. Kong, X. Chen, L. Zhang, X. Hu, M. Mu, H. Sun, X. Shao, X. Guan, M. Gao, B. Xu, Synthesis of SnO2/graphene composite anode materials for lithium-ion batteries, Appl Surf Sci. 485 (2019) 314–322. https://doi.org/10.1016/j.apsusc.2019.04.225.

[31] R. Tian, Y. Zhang, Z. Chen, H. Duan, B. Xu, Y. Guo, H. Kang, H. Li, H. Liu, The effect of annealing on a 3D SnO2/graphene foam as an advanced lithium-ion battery anode, Sci Rep. 6 (2016) 1–9. https://doi.org/10.1038/srep19195.

[32] K. Zhao, L. Zhang, R. Xia, Y. Dong, W. Xu, C. Niu, L. He, M. Yan, L. Qu, L. Mai, SnO 2 Quantum Dots@Graphene Oxide as a High-Rate and Long-Life Anode Material for Lithium-Ion Batteries, Small. 12 (2016) 588–594. https://doi.org/10.1002/smll.201502183.

[33] A. Jahel, C.M. Ghimbeu, L. Monconduit, C. Vix-Guterl, Confined ultrasmall SnO2 particles in micro/mesoporous carbon as an extremely long cycle-life anode material for Li-ion batteries, Adv Energy Mater. 4 (2014). https://doi.org/10.1002/aenm.201400025.

[34] J.S. Chen, X.W. Lou, SnO2-based nanomaterials: Synthesis and application in lithium-ion batteries, Small. 9 (2013) 1877–1893. https://doi.org/10.1002/smll.201202601.

[35] J.H. Harreld, J. Sakamoto, B. Dunn, Non-hydrolytic sol-gel synthesis and electrochemical characterization of tin-based oxide aerogels, J Power Sources. 115 (2003) 19–26. https://doi.org/10.1016/S0378-7753(02)00626-2.

[36] R. Hu, D. Chen, G. Waller, Y. Ouyang, Y. Chen, B. Zhao, B. Rainwater, C. Yang, M. Zhu, M. Liu, Dramatically enhanced reversibility of Li2O in SnO2-based electrodes: The effect of nanostructure on high initial reversible capacity, Energy Environ Sci. 9 (2016) 595–603. https://doi.org/10.1039/c5ee03367e.

[37] X. Chen, H. Lu, Y. Lei, J. Zhang, F. Xiao, R. Wang, P. Xie, J. Xu, Expanded graphite confined SnO2 as anode for lithium ion batteries with low average working potential and enhanced rate capability, J Mater Sci Technol. 107 (2022) 165–171. https://doi.org/10.1016/j.jmst.2021.06.087.

[38] N. Yesibolati, M. Shahid, W. Chen, M.N. Hedhili, M.C. Reuter, F.M. Ross, H.N. Alshareef, SnO2 anode surface passivation by atomic layer deposited HfO2 improves li-ion battery performance, Small. 10 (2014) 2849–2858. https://doi.org/10.1002/smll.201303898.

[39] K. Zhao, L. Zhang, R. Xia, Y. Dong, W. Xu, C. Niu, L. He, M. Yan, L. Qu, L. Mai, SnO2 Quantum Dots@Graphene Oxide as a High-Rate and Long-Life Anode Material for Lithium-Ion Batteries, Small. 12 (2016) 588–594. https://doi.org/10.1002/smll.201502183.

[40] S. Wang, G. Xu, K. Wang, B. Han, Y. Wang, L. Li, D. Ju, M. Chai, D. Zhang, W.M. Zhou, Fabrication and electrochemical performances of SnO2@C composite materials, Current Research in Green and Sustainable Chemistry. 4 (2021) 100099. https://doi.org/10.1016/j.crgsc.2021.100099.

[41] I. Dienwiebel, M. Diehl, B. Heidrich, X. Yang, M. Winter, M. Börner, Enabling Aqueous Processing for LiNi 0.5 Mn 1.5 O 4 -Based Positive Electrodes in Lithium-Ion Batteries by Applying Lithium-Based Processing Additives, Advanced Energy and Sustainability Research. 2 (2021) 2100075. https://doi.org/10.1002/aesr.202100075.

[42] M. Aziz, S. Saber Abbas, W.R. Wan Baharom, Size-controlled synthesis of SnO2 nanoparticles by sol-gel method, Mater Lett. 91 (2013) 31–34. https://doi.org/10.1016/j.matlet.2012.09.079.

[43] C. Gervillié, A. Boisard, J. Labbé, K. Guérin, S. Berthon-Fabry, Relationship between tin environment of SnO2 nanoparticles and their electrochemical behaviour in a lithium ion battery, Mater Chem Phys. 257 (2021). https://doi.org/10.1016/j.matchemphys.2020.123461.

[44] P. Sangeetha, V. Sasirekha, V. Ramakrishnan, Micro-Raman investigation of tin dioxide nanostructured material based on annealing effect, Journal of Raman Spectroscopy. 42 (2011) 1634–1639. https://doi.org/10.1002/jrs.2919.

[45] I.A. Courtney, Electrochemical and In Situ X-Ray Diffraction Studies of the Reaction of Lithium with Tin Oxide Composites, J Electrochem Soc. 144 (1997) 2045. https://doi.org/10.1149/1.1837740.

[46] Y. Surace, F. Jeschull, T. Schott, S. Zürcher, M.E. Spahr, S. Trabesinger, Improving the Cycling Stability of SnO2-Graphite Electrodes, ACS Appl Energy Mater. 2 (2019) 7364–7374. https://doi.org/10.1021/acsaem.9b01344.

[47] J. Wang, H. Zhao, X. Liu, J. Wang, C. Wang, Electrochemical properties of SnO2/carbon composite materials as anode material for lithium-ion batteries, Electrochim Acta. 56 (2011) 6441–6447. https://doi.org/10.1016/j.electacta.2011.04.134.

[48] C. Kim, M. Noh, M. Choi, J. Cho, B. Park, Critical size of a nano SnO2 electrode for Li-secondary battery, Chemistry of Materials. 17 (2005) 3297–3301. https://doi.org/10.1021/cm048003o.

[49] R. Tian, N. Alcala, S.J.K. O'Neill, D. V. Horvath, J. Coelho, A.J. Griffin, Y. Zhang, V. Nicolosi, C. O'Dwyer, J.N. Coleman, Quantifying the Effect of Electronic Conductivity on the Rate Performance of Nanocomposite Battery Electrodes, ACS Appl Energy Mater. 3 (2020) 2966–2974. https://doi.org/10.1021/acsaem.0c00034.

[50] J. Entwistle, R. Ge, K. Pardikar, R. Smith, D. Cumming, Carbon binder domain networks and electrical conductivity in lithium-ion battery electrodes: A critical review, Renewable and Sustainable Energy Reviews. 166 (2022) 112624. https://doi.org/10.1016/j.rser.2022.112624.

[51] B. Lee, S.C. Han, M. Oh, M.S. Lah, K.-S. Sohn, M. Pyo, Tin dioxide nanoparticles impregnated in graphite oxide for improved lithium storage and cyclability in secondary ion batteries, Electrochim Acta. 113 (2013) 149–155. https://doi.org/10.1016/j.electacta.2013.09.093.

[52] S. Dühnen, J. Betz, M. Kolek, R. Schmuch, M. Winter, T. Placke, Toward Green Battery Cells: Perspective on Materials and Technologies, Small Methods. 4 (2020). https://doi.org/10.1002/smtd.202000039.

[53] S.L. Chou, J.Z. Wang, C. Zhong, M.M. Rahman, H.K. Liu, S.X. Dou, A facile route to carbon-coated SnO2 nanoparticles combined with a new binder for enhanced cyclability of Li-ion rechargeable batteries, Electrochim Acta. 54 (2009) 7519–7524. https://doi.org/10.1016/j.electacta.2009.08.006.

[54] X. Zhang, R. Kostecki, T.J. Richardson, J.K. Pugh, P.N. Ross, Electrochemical and Infrared Studies of the Reduction of Organic Carbonates, J Electrochem Soc. 148 (2001) A1341. https://doi.org/10.1149/1.1415547.

[55] C.C. Nguyen, T. Yoon, D.M. Seo, P. Guduru, B.L. Lucht, Systematic Investigation of Binders for Silicon Anodes: Interactions of Binder with Silicon Particles and Electrolytes and Effects of Binders on Solid Electrolyte Interphase Formation, ACS Appl Mater Interfaces. 8 (2016) 12211–12220. https://doi.org/10.1021/acsami.6b03357.

[56] P. Jehnichen, K. Wedlich, C. Korte, Degradation of high-voltage cathodes for advanced lithium-ion batteries–differential capacity study on differently balanced cells, Sci Technol Adv Mater. 20 (2019) 1–9. https://doi.org/10.1080/14686996.2018.1550625.

[57] J.H. Kim, N.P.W. Pieczonka, Z. Li, Y. Wu, S. Harris, B.R. Powell, Understanding the capacity fading mechanism in LiNi0.5Mn 1.5O4/graphite Li-ion batteries, Electrochim Acta. 90 (2013) 556–562. https://doi.org/10.1016/j.electacta.2012.12.069.

[58] J. Kasnatscheew, T. Placke, B. Streipert, S. Rothermel, R. Wagner, P. Meister, I.C. Laskovic, M. Winter, A Tutorial into Practical Capacity and Mass Balancing of Lithium Ion Batteries, J Electrochem Soc. 164 (2017) A2479–A2486. https://doi.org/10.1149/2.0961712jes.

[59] J. Asenbauer, J.R. Binder, F. Mueller, M. Kuenzel, D. Geiger, U. Kaiser, S. Passerini, D. Bresser, Scalable Synthesis of Microsized, Nanocrystalline Zn0.9Fe0.1O-C Secondary Particles and Their Use in Zn0.9Fe0.1O-C/LiNi0.5Mn1.5O4 Lithium-Ion Full Cells, ChemSusChem. 13 (2020) 3504–3513. https://doi.org/10.1002/cssc.202000559.

[60] A. Birrozzi, J. Asenbauer, T.E. Ashton, A.R. Groves, D. Geiger, U. Kaiser, J.A. Darr, D. Bresser, Tailoring the Charge/Discharge Potentials and Electrochemical Performance of SnO2 Lithium-Ion Anodes by Transition Metal Co-Doping, Batter Supercaps. 3 (2020) 284–292. https://doi.org/10.1002/batt.201900154.

[61] D. Wei, S. Zhong, H. Zhang, X. Zhang, C. Zhu, J. Duan, L. Li, Z. Chen, P. Liu, G. Zhang, H. Duan, In situ construction of interconnected SnO2/nitrogen-doped Carbon@TiO2 networks for lithium-ion half/full cells, Electrochim Acta. 290 (2018) 312–321. https://doi.org/10.1016/j.electacta.2018.08.094.

[62] F. Li, G. Wang, D. Zheng, X. Zhang, C.J. Abegglen, H. Qu, D. Qu, Controlled prelithiation of sno2/c nanocomposite anodes for building full lithium-ion batteries, ACS Appl Mater Interfaces. 12 (2020) 19423–19430. https://doi.org/10.1021/acsami.0c00729.

[63] N. Kamboj, B. Debnath, S. Bhardwaj, T. Paul, N. Kumar, S. Ogale, K. Roy, R.S. Dey, Ultrafine Mix-Phase SnO-SnO $_2$ Nanoparticles Anchored on Reduced Graphene Oxide Boost Reversible Li-Ion Storage Capacity beyond Theoretical Limit, ACS Nano. 16 (2022) 15358–15368. https://doi.org/10.1021/acsnano.2c07008.

[64] Y. Wang, N. Jiang, D. Pan, H. Jiang, Y. Hu, C. Li, Controllable oxygen vacancy SnO2-x anodes for lithium-ion batteries with high stability, Chemical Engineering Journal. 437 (2022) 135422. https://doi.org/10.1016/j.cej.2022.135422.

[65] J. Long, T. Han, Y. Ding, C. Hu, J. Liu, Co-coating ZnCo2O4 and carbon on a biomimetic sea anemone-shaped SnO2 mesostructure for high-performance lithium-ion batteries and semi-solid lithium slurry batteries, Appl Surf Sci. 591 (2022) 153220. https://doi.org/10.1016/j.apsusc.2022.153220.

[66] M. Tu, L. Yu Ruixin Jia, X. Kong, R. Zhang, B. Xu, Chitosan modulated engineer tin dioxide nanoparticles well dispersed by reduced graphene oxide for high and stable lithium-ion storage, J Colloid Interface Sci. 635 (2023) 105–116. https://doi.org/10.1016/j.jcis.2022.12.126.

[67] H. Song, K. Tian, Z. Fang, C. Guan, H. Jiang, M. Lu, M. Zhang, S. Zhuang, H. Wei, D. Wei, X. Li, Steric-hindrance effect and self-sacrificing template behavior induced PDA@SnO2-QDs/N-doped carbon hollow nanospheres: Enhanced structural stability and reaction kinetics for long-cyclic Li-ion half/full batteries, J Colloid Interface Sci. 631 (2023) 214–223. https://doi.org/10.1016/j.jcis.2022.11.035.

[68] G. Wen, H. Liu, T. Liang, Y. Ouyang, L. Tan, R. Hu, J. Liu, Y. Zhang, M. Zhu, Good cycling stability and high initial efficiency demonstrated in full cells with limited lithium source for an advanced SnO2–Co–C composite anode, Electrochim Acta. 334 (2020) 135640. https://doi.org/10.1016/j.electacta.2020.135640.

[69] D. Wei, S. Zhong, H. Zhang, X. Zhang, C. Zhu, J. Duan, L. Li, Z. Chen, P. Liu, G. Zhang, H. Duan, In situ construction of interconnected SnO2/nitrogen-doped Carbon@TiO2 networks for lithium-ion half/full cells, Electrochim Acta. 290 (2018) 312–321. https://doi.org/10.1016/j.electacta.2018.08.094.

[70] X. Yang, Y. Huang, M. Wang, Z. Miao, H. Liu, Z. Chen, Z. Yang, J. Yu, Double hollow Zn2SnO4/SnO2@N-doped carbon nanocubes as anode material for High-performance Li-ion batteries, Chem Phys Lett. 813 (2023) 140285. https://doi.org/10.1016/j.cplett.2022.140285.

[71] Z. Cui, F. Zou, H. Celio, A. Manthiram, Paving Pathways Toward Long-Life Graphite/LiNi 0.5 Mn 1.5 O 4 Full Cells: Electrochemical and Interphasial Points of View, Adv Funct Mater. 32 (2022) 2203779. https://doi.org/10.1002/adfm.202203779.

827 **Figures Captions**

828 **Figure 1:** TEM micrographs of SnO_2-400 a), SnO_2-700 b), SnO_2-900 c) and SnO_2-1000
829 d).

830 **Figure 2:** a) XRD analysis of SnO_2-400, SnO_2-700, SnO_2-900, SnO_2-1000, commercial
831 SnO_2 and the reference pattern of SnO_2 (code: 98-015-7448); b) Raman analysis of SnO_2-
832 400, SnO_2-700, SnO_2-900, SnO_2-1000.

833 **Figure 3:** Specific capacity vs cycle number plot of SnO_2-400 cells. Lithiation testing
834 protocol: first three cycles at C/10 followed by cycling at 1C and last three cycles at C/10.
835 De-lithiation at 1C. Electrodes are prepared with different weight ratio of the components
836 SnO_2-400: carbon black: PVdF: (a) 40:50:10, (b) 50:40:10, (c) 60:30:10 and (d) 70:20:10.

837 **Figure 4:** Specific capacity vs cycle number plot of a) SnO_2-400 with different binders
838 (aqueous slurry with CMC and NMP slurry with PVdF). Galvanostatic cycling comprises
839 formation at C/10 followed by 100 cycles at 1C (lithiation process). De-lithiation is
840 carried out at 1C. SnO_2: carbon black: binder ratio is 70:20:10; b) voltage profiles and c)
841 dQ/dV plots of the 1^{st} and 2^{nd} cycles.

842 **Figure 5:** Specific capacity vs cycle number plot of a) SnO_2/LNMO full cell in the
843 potential range of 2.5 - 4.9V vs. Li^+/Li and b) correspondent voltage vs capacity plots.
844 Voltage vs time plots of the full cell, cathode and anode measured towards Li reference
845 electrode.

846 **Figure 6:** Voltage vs capacity plots of a) recovered LNMO in the half cell, b) pristine
847 LNMO in the half cell, c) specific capacity vs cycle number of recovered LNMO in the
848 half cell. Voltage vs capacity plots of d) recovered SnO_2 in the half cell, e) pristine SnO_2
849 in the half cell, f) specific capacity vs cycle number of recovered SnO_2 in the half cell.